REPORT

CATALYSIS

Maximizing noble metal utilization in solid catalysts by control of nanoparticle location

Kang Cheng[1,2]†, Luc C. J. Smulders[1]†, Lars I. van der Wal[1], Jogchum Oenema[1], Johannes D. Meeldijk[1,3], Nienke L. Visser[1], Glenn Sunley[4], Tegan Roberts[4], Zhuoran Xu[5], Eric Doskocil[5], Hideto Yoshida[1,6], Yanping Zheng[2], Jovana Zečević[1], Petra E. de Jongh[1], Krijn P. de Jong[1]*

Maximizing the utilization of noble metals is crucial for applications such as catalysis. We found that the minimum loading of platinum for optimal performance in the hydroconversion of *n*-alkanes for industrially relevant bifunctional catalysts could be reduced by a factor of 10 or more through the rational arranging of functional sites at the nanoscale. Intentionally depositing traces of platinum nanoparticles on the alumina binder or the outer surface of zeolite crystals, instead of inside the zeolite crystals, enhanced isomer selectivity without compromising activity. Separation between platinum and zeolite acid sites preserved the metal and acid functions by limiting micropore blockage by metal clusters and enhancing access to metal sites. Reduced platinum nanoparticles were more active than platinum single atoms strongly bonded to the alumina binder.

Noble metals (NMs) are widely used in a variety of commercial and emerging technologies, including catalytic converters in automobiles; electrocatalysts in hydrogen fuel cells; and catalysts for petroleum, biomass, and waste conversion (*1*–*5*). Increasing demand for NMs in these applications is driving approaches that make more efficient use of NMs (*6*–*9*), including so-called single-atom catalysts (SACs) in which isolated single metal atoms or ions are stabilized by the support (*10*–*13*). However, strong metal-support interactions often lead to limited reducibility and in some cases low reactivity. Confinement of NMs inside zeolite channels or cages can benefit the adsorption of reagents and stabilization of reaction intermediates to improve catalytic activity, product selectivity, or both (*14*–*16*). Successful examples of confinement effects have been demonstrated for the conversion of small molecules, including carbon monoxide (CO) oxidation, methane (CH_4) oxidation, and the water-gas shift reaction (*17*–*19*).

In the petrochemical industry, platinum (Pt) is frequently used in combination with acidic zeolites for the hydroconversion of linear alkanes to enhance the quality of liquid fuels (fig. S1), and its performance is influenced by the Pt nanoparticle (NP) size and distribution, metal-support interactions, and acidic properties (*20*–*23*). To describe the required Pt loading sufficient to maintain the bifunctional metal-acid balance in hydroconversion catalysts, Guisnet and coworkers proposed a widely applied parameter of the surface Pt sites to Brønsted acid sites ratio (n_{pt}/n_a) (*24*). To meet this criterion, the typical Pt loading for bifunctional catalysts is in the range of 0.3 to 3 wt % (*25*–*27*). For integrating two functional components, Weisz's intimacy criterion, which is often interpreted as "the closer the better," has been applied to spatial organization (*28*). Recently, we have shown at Pt loadings around 0.5 wt % that separation of Pt and acid sites at the nanoscale enhanced the isomer selectivity in hydroisomerization of linear alkanes, whereas placing Pt inside zeolite crystals with closest proximity promoted acid-catalyzed cracking or overcracking reactions because of the high concentrations of intracrystalline carbenium ions (*29*–*31*). With this concept of nanoscale intimacy, we found that lowering the Pt loading holds potential (*30*), which inspired us to study the lower limit of NMs for catalysis as a function of the Pt NP location.

We controlled the Pt location and loading on industrially relevant platinum-zeolite-alumina (Al_2O_3) composite catalysts to decrease the Pt loading for hydroisomerization while maintaining optimal performance. We used *n*-heptane as a model molecule relevant to gasoline upgrading. We used the one-dimensional (1D) zeolites HZSM-22 and HMOR to construct bifunctional catalysts (tables S1 and S2 and fig. S2). To provide mechanical stability and to avoid the high-pressure drop in industrial fixed-bed reactors, zeolite catalysts need to be shaped into composites—for example, as extrudates with the use of a binder such as clay (*32*). The location of Pt sites in these composite catalysts can be roughly classified into three types: (i) on the outer surface of zeolite crystals; (ii) inside the zeolite crystals; and (iii) on the binder (fig. S3). We controlled the Pt location on the composite catalysts through either ion exchange (IE) by using $Pt(NH_3)_4(NO_3)_2$ as Pt precursor or ion adsorption (IA) by using H_2PtCl_6 (fig. S4). The actual weight loading of Pt was determined by means of inductively coupled plasma (ICP) spectrometry (tables S3 and S4). Because all raw materials are based on commercial products and the IE and IA methods are commonly applied in industry, no major barriers are foreseen for the catalyst preparation on a large scale.

High-angle annular dark-field scanning transmission electron microscopy (HAADF-STEM) imaging combined with ultramicrotomy can expose cross sections of zeolite crystals or shaped catalysts and enables the visualization of the spatial distribution of Al_2O_3 binder, zeolite crystals, and Pt sites (*29*). The zeolite-Al_2O_3 composite, by use of acetic acid as a peptizing agent in this work, exhibited a uniform distribution of zeolite crystals, which were coated and stabilized by the Al_2O_3 binder (Fig. 1A). By contrast, large agglomerates of zeolites and Al_2O_3 were observed over zeolite+Al_2O_3 composite without acetic acid (fig. S5). Because the kinetic diameter of the $Pt(NH_3)_4^{2+}$ (0.48 nm) is comparable with the HZSM-22 pore size (0.45 by 0.55 nm) and HMOR pore size (0.67 by 0.70 nm), the diffusion of $Pt(NH_3)_4^{2+}$ ions into the micropores during the IE process could be limited. The STEM images of Pt-HZSM-22 slices confirmed that after reduction, most Pt NPs were present on the external crystal surfaces, regardless of the Pt loading, and a small fraction was located inside the HZSM-22 crystals (Fig. 1B). The average sizes of Pt NPs for 0.2Pt-HZSM-22 (where 0.2 is Pt loading in weight percent) and 1.0Pt-HZSM-22 were 1.5 and 1.7 nm, respectively. For 0.2Pt-HMOR and 1.0Pt-HMOR, the average diameters of Pt NPs were 1.2 and 1.6 nm, respectively, and the Pt NPs were exclusively deposited inside HMOR crystals (Fig. 1C). The Pt NPs were larger than the micropores of the zeolite and were likely accommodated by the local destruction of micropores during NP growth, an effect confirmed in previous studies (*33*).

The zeolite powders containing Pt NPs were then mixed with boehmite and acetic acid to prepare bifunctional catalysts with a zeolite-to-Al_2O_3 weight ratio of 1/1. The TEM imaging revealed that for IE-prepared Pt-HZSM-22/Al_2O_3, most Pt NPs remained on the HZSM-22 crystal surfaces with only a few NPs inside the

[1]Materials Chemistry and Catalysis, Debye Institute for Nanomaterials Science, Utrecht University, 3584 CG Utrecht, Netherlands. [2]State Key Laboratory of Physical Chemistry of Solid Surfaces, College of Chemistry and Chemical Engineering, Xiamen University, Xiamen 361005, China. [3]Electron Microscopy Centre, Utrecht University, 3584 CG Utrecht, Netherlands. [4]Applied Sciences, bp Innovation and Engineering, BP plc, Saltend, Hull HU12 8DS, UK. [5]Applied Sciences, bp Innovation and Engineering, BP plc, Naperville, IL 60563, USA. [6]The Institute of Scientific and Industrial Research, Osaka University, 8-1 Mihogaoka, Ibaraki, Osaka 567-0047, Japan.
*Corresponding author. Email: k.p.dejong@uu.nl
†These authors contributed equally to this work.

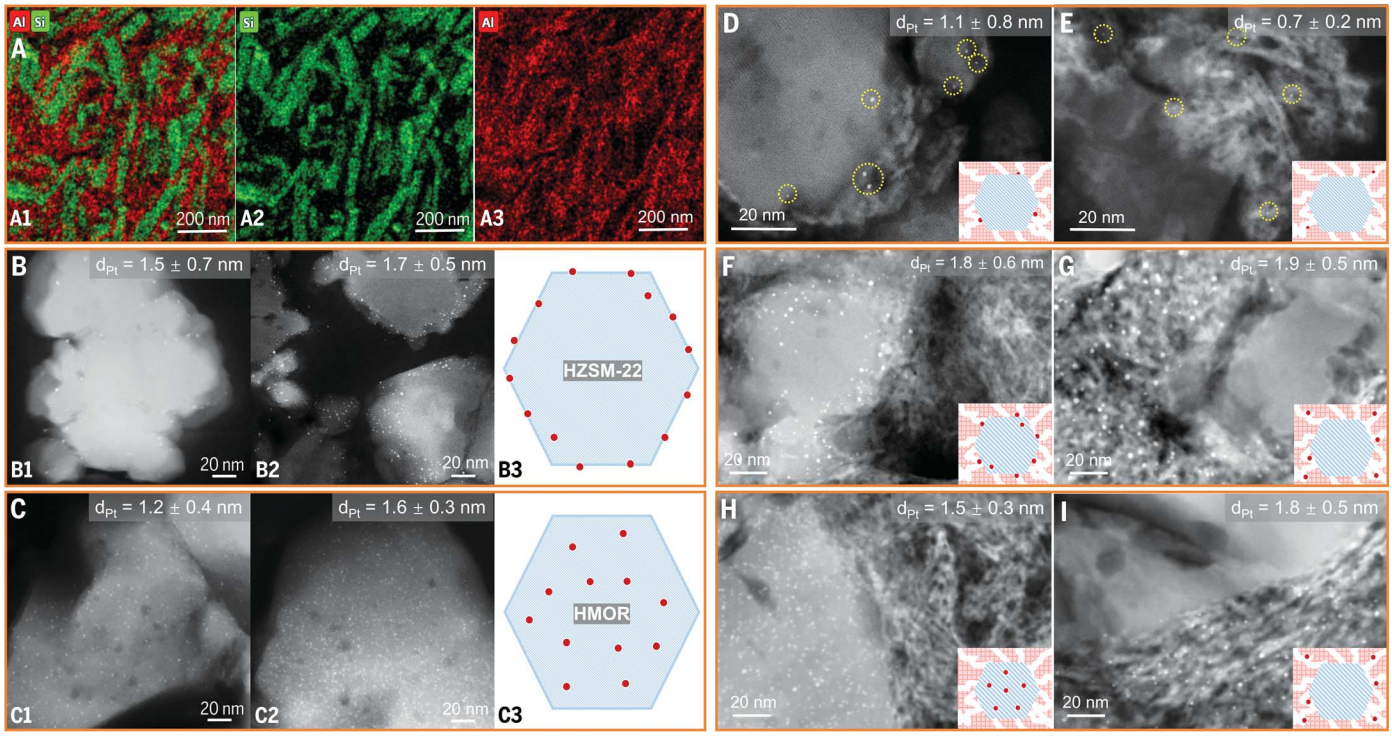

Fig. 1. HAADF-STEM and STEM–energy-dispersive x-ray (EDX) images of ultramicrotomed 70-nm-thick sections of catalysts. (**A**) HZSM-22/Al_2O_3 composite by using acetic acid as a peptizing agent. The images (A1) to (A3) show the location of silicon (green) and aluminum (red), which is indicative of the presence of the HZSM-22 and Al_2O_3 components. (**B**) (B1) 0.2Pt-HZSM-22, (B2) 1.0Pt-HZSM-22, and (B3) scheme for Pt distribution over HZSM-22. (**C**) (C1) 0.2Pt-HMOR, (C2) 1.0Pt-HMOR, and (C3) scheme for Pt distribution over HMOR. (**D** and **E**) 0.01Pt-HZSM-22/Al_2O_3 and 0.01Pt-Al_2O_3/HZSM-22, respectively. (**F** and **G**) 0.5Pt-HZSM-22/Al_2O_3 and 0.5Pt-Al_2O_3/HZSM-22, respectively. (**H** and **I**) 0.5Pt-HMOR/Al_2O_3 and 0.5Pt-Al_2O_3/HMOR, respectively. In the schematic representations, the red dots and blue hexagons indicate Pt NPs and zeolite crystals, respectively.

HZSM-22 crystals, and those NPs were near NPs present on HZSM-22 surfaces; no NPs were observed on the mesoporous Al_2O_3 binder (Fig. 1, D and F, and fig. S6A). Conversely, almost all of the Pt NPs were located on the Al_2O_3 binder for Pt-Al_2O_3/HZSM-22 prepared with the IA method (Fig. 1, E and G, and fig. S6B). Correspondingly, the Pt NPs were still exclusively present inside the HMOR crystals for IE-prepared Pt-HMOR/Al_2O_3 (Fig. 1H), and all of the Pt NPs were deposited on the Al_2O_3 binder for IA-prepared Pt-Al_2O_3/HMOR (Fig. 1I). With this methodology, we prepared a series of composite catalysts with different Pt loadings and locations (table S4). The Pt loading in all cases had a minor effect on the catalyst acidity (fig. S7).

The catalytic performance of HZSM-22–based catalysts in the hydroisomerization of *n*-C_7 was strongly affected by the Pt loading and distribution, especially at loading of 0.005 to 0.05 wt % (Fig. 2 and fig. S8). With an increase of Pt loading, the *n*-C_7 conversion compared at identical temperature and weight hourly space velocity (WHSV) increased first and then reached a plateau. Unexpectedly, with the Pt-on–HZSM-22 configuration, an ultralow Pt loading of 0.01 wt % was sufficient to maintain the *n*-C_7 conversion and selectivity of C_7 isomers (Fig. 2A). Such a low Pt loading is usually insufficient for catalyzing this reaction. However, 0.01Pt-Al_2O_3/HZSM-22 exhibited inferior activity and selectivity (Fig. 2B). The C_7 isomers consisted of monobranched and traces of dibranched C_7 isomers (mono-C_7 and di-C_7, respectively), and the main side products were propane, *n*-butane, and *iso*-butane from acid-catalyzed hydrocracking (*30*).

At similar conversion levels, 0.01Pt-HZSM-22/Al_2O_3 also provided higher selectivity of C_7 isomers than did 0.01Pt-Al_2O_3/HZSM-22 (fig. S9). Increasing the Pt loading >0.01 wt % decreased the selectivity of C_7 isomers, which was likely the result of more Pt NPs sited in the pore mouth region of HZSM-22, which would promote cracking reactions (*30*). For Pt-Al_2O_3/HZSM-22 with Pt-on-Al_2O_3, both the *n*-C_7 conversion and selectivity of C_7 isomers increased steadily and then reached a plateau as Pt loading increased to 0.05 wt % (Fig. 2B). With Pt-on-binder, therefore, a minimum loading of 0.05 wt % was required to sustain the *n*-heptane conversion and the selectivity of C_7 isomers, to ensure the equilibrium of the dehydrogenation-hydrogenation reactions.

Over HMOR-based catalysts, both the *n*-C_7 conversion and the selectivity of C_7 isomers increased with the Pt loading, and overall, the performance of catalysts with Pt inside HMOR crystals was more strongly influenced by the Pt loading (Fig. 2, C and D, and fig. S8). At the same Pt loading, the specific *n*-C_7 conversion over Pt-HMOR/Al_2O_3 was lower than the corresponding Pt-Al_2O_3/HMOR, probably because of pore blockage or poor accessibility of Pt NPs (*34*). With a 10-fold increase of Pt loading from 0.05 to 0.5%, the *n*-C_7 conversion increased from 58 to 71% with a selectivity of C_7 isomers ~80% over Pt-Al_2O_3/HMOR, whereas the *n*-C_7 conversion increased from 22 to 67% and the selectivity of C_7 isomers increased from 28 to 72% over Pt-HMOR/Al_2O_3. Regardless of the Pt loading and location over the composite catalysts, after more than 100 hours, we observed virtually no catalyst deactivation for both HZSM-22– and HMOR-based catalysts (figs. S10 and S11).

The dependence of the maximum yield of C_7 isomers, an important performance indicator in alkane hydroisomerization (*26*), on the platinum loading is summarized in Fig. 3. The acid density of HMOR is much higher than that of HZSM-22. Therefore, HMOR-based

catalysts required more Pt sites to obtain the same n_{Pt}/n_a ratio (fig. S12). A composite catalyst with Pt-on–HZSM-22 exhibited an optimum loading of only 0.01 wt % for maximizing the yield of C_7 isomers (≈64%) (Fig. 3A). For Pt-Al_2O_3/HZSM-22 with Pt-on-binder, the increase of Pt loading above 0.05 wt % maximized the yield of C_7 isomers toward 68%. Likewise, the maximum yield of C_7 isomers for Pt-Al_2O_3/HMOR went up with Pt loading, and relative to HZSM-22, a much higher loading of Pt (≈0.1 wt %) was needed to provide maximum yields of C_7 isomers (Fig. 3B). Disadvantageous for the yield of C_7 isomers was to confine the Pt inside HMOR crystals, which promoted the cracking reaction and prevented the conversion of n-C_7. The maximum yield of C_7 isomers over 0.05Pt-Al_2O_3/HMOR was near that over 0.5Pt-HMOR/Al_2O_3, suggesting that a rational placement of Pt could lead to a 10-fold reduction in its usage.

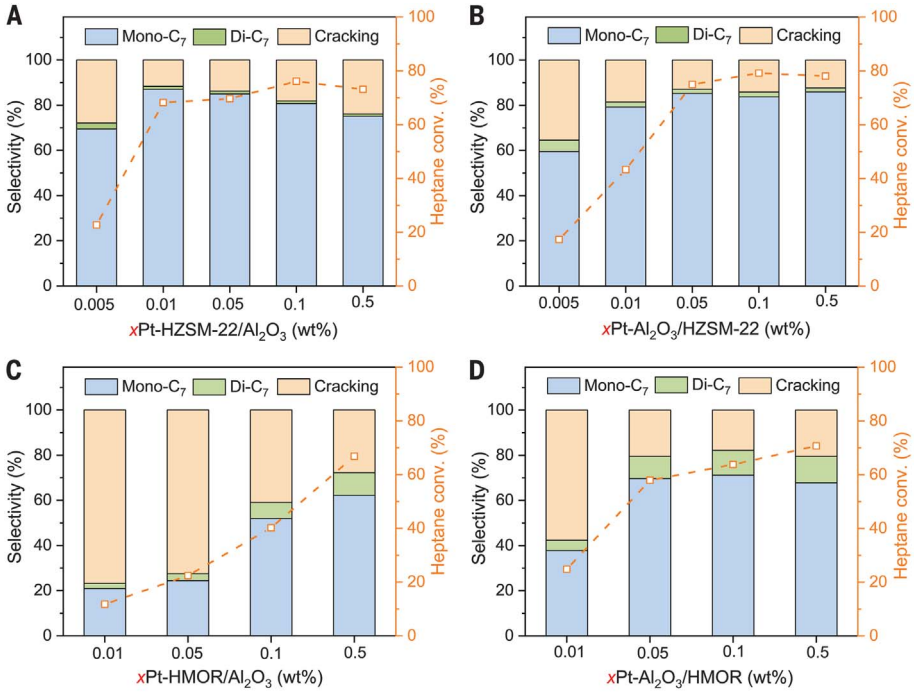

Fig. 2. Hydroconversion of *n*-heptane over bifunctional catalysts with different Pt loadings and locations. (**A**) Pt-HZSM-22/Al_2O_3 with Pt on the HZSM-22 crystals and (**B**) Pt-Al_2O_3/HZSM-22 with Pt on the Al_2O_3 binder. Data are partly from (*30*). (**C**) Pt-HMOR/Al_2O_3 with Pt inside the HMOR crystals and (**D**) Pt-Al_2O_3/HMOR with Pt on the Al_2O_3 binder. Data are partly from (*30*). Reaction conditions were pressure (P) = 10 bar, H_2/n-C_7 = 10/1, WHSV = 2.1 $g_{n\text{-}C7}$ g_{cat}^{-1} $hour^{-1}$, and temperature (T) = 320°C for HZSM-22–based catalysts and T = 270°C for HMOR-based catalysts.

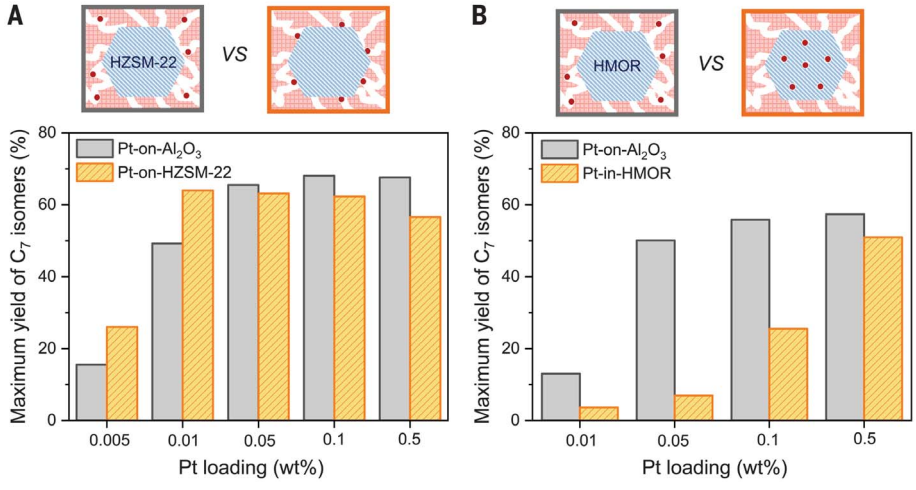

Fig. 3. The effect of Pt loading on the maximum yield of C_7 isomers. (**A**) Pt–HZSM-22–Al_2O_3 composite catalysts, with Pt NPs placed either on Al_2O_3 binder or on HZSM-22 crystals, and (**B**) Pt-HMOR-Al_2O_3, with Pt NPs placed either on Al_2O_3 binder or inside HMOR crystals. Reaction conditions were P = 10 bar, H_2/n-C_7 = 10/1, and WHSV = 2.1 $g_{n\text{-}C7}$ g_{cat}^{-1} $hour^{-1}$. The red dots and blue hexagons indicate Pt NPs and zeolite crystals, respectively.

In the low loading range (≤0.01 wt %), Pt placed on the Al_2O_3 binder was less effective than on HZSM-22 crystals (Figs. 2, A and B, and 3A). Highly dispersed Pt sites stabilized by the alumina (Pt–O–Al) could be difficult to reduce and not be sufficiently active for dehydrogenation of n-heptane. To investigate this, we intentionally prepared a SAC-Pt-Al_2O_3/HMOR catalyst with single-atom Pt dispersed on Al_2O_3, which was almost inactive in n-heptane hydroconversion (fig. S13). The x-ray absorption spectroscopy (XAS) shows the k^2-weighted (where k is photo-electron wave number), phase-corrected extended x-ray absorption fine structure (EXAFS) spectra of reduced Pt catalysts together with Pt standards (Fig. 4A). The scattering from the first shell of Pt–O led to the peak below 2.0 Å, whereas the scattering Pt–Pt in the Pt foil resulted in peaks at 2.4 and 2.9 Å (*7*). The scattering peak at 2.2 Å observed with a bond distance shorter than that of Pt–Pt may indicate the formation of Pt dimers (*35*).

Strong Pt–Pt scattering for 0.1Pt-HMOR and 0.1Pt-HZSM-22 with 0.1 wt % loadings could be observed (Fig. 4A), which is indicative of the formation of metallic Pt NPs or clusters. A Pt–O scattering peak was observed over 0.01Pt-HZSM-22/Al_2O_3 and 0.01Pt-Al_2O_3/HZSM-22, indicating that single-atom Pt (ions) was present within the two samples together with Pt NPs observed with electron microscopy (Fig. 1, D and E). More than half of Pt was metallic over 0.01Pt-HZSM-22/Al_2O_3, which exhibited higher reactivity in n-C_7 conversion than that of 0.01Pt-Al_2O_3/HZSM-22 that contained mainly oxidized Pt (fig. S14 and table S5). As the Pt loading on the Al_2O_3 binder increased from 0.01 to 0.05 wt %, the Pt–O scattering became negligible, and Pt–Pt scattering appeared, which suggested the formation of larger numbers of small Pt NPs or clusters in line with electron microscopy results (Fig. 1). The in situ x-ray photoelectron spectroscopy (Fig. 4B) further suggested reduced 0.1Pt-HZSM-22/Al_2O_3 and 0.1Pt-Al_2O_3/HZSM-22 to mainly contain metallic Pt (313.7 eV), whereas the atomically dispersed Pt on Al_2O_3 (SAC-0.2Pt-Al_2O_3) was in a partially oxidized state (314.6 eV) (*36*). The weaker Pt signals of 0.1Pt-HZSM-22/Al_2O_3 than those of 0.1Pt-Al_2O_3/HZSM-22 imply that a fraction of Pt NPs might be confined in the micropores of HZSM-22, causing cracking reactions at high (≥0.1 wt %) Pt loadings (Fig. 2A).

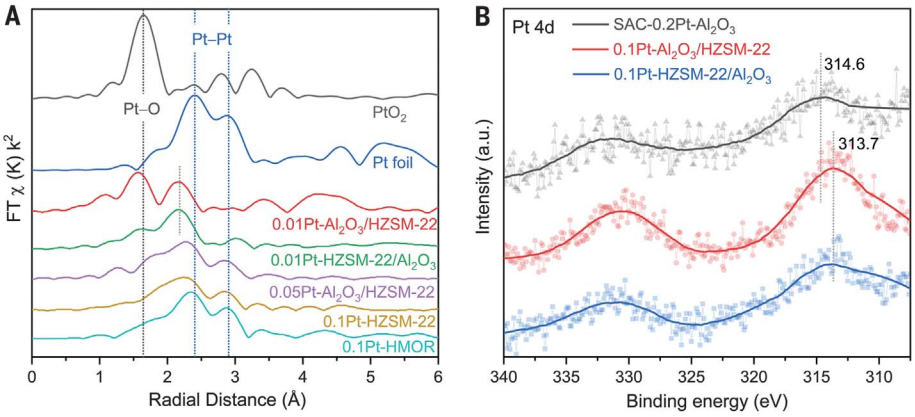

Fig. 4. Chemical state of Pt. (**A**) The k^2-weighted Pt L_3 edge EXAFS spectra in R space of bifunctional catalysts. Catalysts were reduced under 3.5 vol % H_2 flow at 350°C for 1 hour. PtO_2 and Pt foil were used as Pt standards. (**B**) In situ XPS spectra of reduced catalysts.

To increase the Pt utilization over bifunctional Pt-zeolite catalysts, we have varied the proximity between sites by controlling the spatial distribution of Pt NPs. Because of the low diffusivity of alkanes and alkenes, Pt sites should be placed in an accessible location in solid catalysts rather than in the micropores of a zeolite, such as on a mesoporous alumina binder or the outer surface of the zeolite crystals. Additionally, maintaining a separation between Pt and zeolite acid sites can preserve the metal and acid functions to the greatest extent through three main mechanisms: (i) limiting micropore blockage by metal clusters, (ii) enhancing accessibility of metal sites, and (iii) favoring pore mouth catalysis to reduce secondary cracking reactions (*29*). Furthermore, reducible Pt ensemble sites were confirmed to be more active as the dehydrogenation-hydrogenation function than Pt SAC, which was strongly bonded by the alumina binder, especially at low platinum loadings. Our findings generally agree with the classical criterion that a minimum amount of NMs is necessary to maintain the metal-acid balance and ensure a quasi-equilibration of the dehydrogenation-hydrogenation reactions, but this study confirms that the required loading for NMs is profoundly affected by how functional sites are arranged at the nanoscale.

REFERENCES AND NOTES

1. A. Wang, J. Li, T. Zhang, *Nat. Rev. Chem.* **2**, 65–81 (2018).
2. L. Chong *et al.*, *Science* **362**, 1276–1281 (2018).
3. R. T. Hannagan *et al.*, *Science* **372**, 1444–1447 (2021).
4. F. Zhang *et al.*, *Science* **370**, 437–441 (2020).
5. Z. Huang *et al.*, *Nat. Catal.* **3**, 170–178 (2020).
6. L. DeRita *et al.*, *Nat. Mater.* **18**, 746–751 (2019).
7. H. Jeong *et al.*, *Nat. Catal.* **3**, 368–375 (2020).
8. K. D. Rasmussen, H. Wenzel, C. Bangs, E. Petavratzi, G. Liu, *Environ. Sci. Technol.* **53**, 11541–11551 (2019).
9. A. E. Hughes, N. Haque, S. A. Northey, S. Giddey, *Resources* **10**, 93 (2021).
10. B. Qiao *et al.*, *Nat. Chem.* **3**, 634–641 (2011).
11. S. Mitchell, E. Vorobyeva, J. Pérez-Ramírez, *Angew. Chem. Int. Ed.* **57**, 15316–15329 (2018).
12. Z. Li *et al.*, *Chem. Rev.* **120**, 623–682 (2020).
13. H. Xiong, A. K. Datye, Y. Wang, *Adv. Mater.* **33**, e2004319 (2021).
14. J. D. Kistler *et al.*, *Angew. Chem. Int. Ed.* **53**, 8904–8907 (2014).
15. N. Kosinov, C. Liu, E. J. M. Hensen, E. A. Pidko, *Chem. Mater.* **30**, 3177–3198 (2018).
16. L. Liu *et al.*, *Nat. Mater.* **18**, 866–873 (2019).
17. S. M. Wu, X. Y. Yang, C. Janiak, *Angew. Chem. Int. Ed.* **58**, 12340–12354 (2019).
18. J. Zhang *et al.*, *Nat. Catal.* **1**, 540–546 (2018).
19. Z. Jin *et al.*, *Science* **367**, 193–197 (2020).
20. L. Liu, A. Corma, *Chem. Rev.* **118**, 4981–5079 (2018).
21. B. Zhang *et al.*, *J. Am. Chem. Soc.* **141**, 8185–8197 (2019).
22. T. W. van Deelen, C. Hernández Mejía, K. P. de Jong, *Nat. Catal.* **2**, 955–970 (2019).
23. L. I. van der Wal *et al.*, *ACS Catal.* **11**, 3842–3855 (2021).
24. G. E. Giannetto, G. R. Perot, M. R. Guisnet, *Ind. Eng. Chem. Prod. Res. Dev.* **25**, 481–490 (1986).
25. A. C. M. van den Broek, J. van Grondelle, R. A. van Santen, *J. Catal.* **167**, 417–424 (1997).
26. J. A. Martens *et al.*, *ChemSusChem* **6**, 421–425 (2013).
27. Z. Guo *et al.*, *Angew. Chem. Int. Ed.* **59**, 1548–1551 (2020).
28. P. B. Weisz, E. W. Swegler, *Science* **126**, 31–32 (1957).
29. J. Zečević, G. Vanbutsele, K. P. de Jong, J. A. Martens, *Nature* **528**, 245–248 (2015).
30. K. Cheng *et al.*, *Angew. Chem. Int. Ed.* **59**, 3592–3600 (2020).
31. J. Oenema *et al.*, *ACS Catal.* **10**, 14245–14257 (2020).
32. N. L. Michels, S. Mitchell, J. Pérez-Ramírez, *ACS Catal.* **4**, 2409–2417 (2014).
33. J. Zečević, A. M. J. van der Eerden, H. Friedrich, P. E. de Jongh, K. P. de Jong, *ACS Nano* **7**, 3698–3705 (2013).
34. M. Guisnet, F. Alvarez, G. Giannetto, G. Perot, *Catal. Today* **1**, 415–433 (1987).
35. U. Müller, K. Sattler, J. Xhie, N. Venkateswaran, G. Raina, *Z. Phys. D At. Mol. Clust.* **19**, 319–321 (1991).
36. T. Huizinga, H. F. J. van 't Blik, J. C. Vis, R. Prins, *Surf. Sci.* **135**, 580–596 (1983).

ACKNOWLEDGMENTS

N. Nikolopoulos, G. Totarella, and S. Zanoni are acknowledged for measuring and analyzing the N_2 physisorption data. **Funding:** This work has been supported by BP plc and Topsector Chemie consortia for Knowledge and Innovation (TKIs). K.P.d.J. acknowledges funding from the European Research Council (ERC), EU FP7 ERC Advanced Grant 338846. K.C. thanks the support from the National Key Research and Development Program of Ministry of Science and Technology 2020YFB0606401. H.Y. thanks the Program for Advancing Strategic International Networks to Accelerate the Circulation of Talented Researchers by JSPS. **Author contributions:** K.C. conducted the catalyst preparation; catalytic evaluation; sample characterizations by NH_3-TPD, SEM, and XRF; and drafted the manuscript. L.C.J.S. assessed the catalyst stability, performed additional characterizations, and helped revise the manuscript. L.I.v.d.W., J.D.M., N.L.V., and H.Y. performed STEM imaging. J.O. guided the catalyst preparation and maintained the reaction unit. G.S., T.R., P.E.d.J., and J.Z. contributed to the discussion of all the results. Z.X. and E.D. performed the XAS measurements and analyzed the data. Y.Z. performed XPS analysis. K.P.d.J. initiated and supervised the project and manuscript writing. All authors approved the final version of the manuscript. **Competing interests:** The authors declare no competing interests. **Data and materials availability:** All data and images are available in the manuscript or supplementary materials.

SUPPLEMENTARY MATERIALS

science.org/doi/10.1126/science.abn8289
Materials and Methods
Supplementary Text
Figs. S1 to S14
Tables S1 to S5
References (*37*–*40*)

Submitted 11 January 2022; resubmitted 24 March 2022
Accepted 18 May 2022
10.1126/science.abn8289